ADVANCED ENERGY MATERIALS
www.advenergymat.de

Synergistic Effect of Bimetallic MOF Modified Separator for Long Cycle Life Lithium-Sulfur Batteries

Rameez Razaq, Mir Mehraj Ud Din, Didrik Rene Småbråten, Volkan Eyupoglu, Saravanan Janakiram, Tor Olav Sunde, Nima Allahgoli, Daniel Rettenwander, and Liyuan Deng**

Severe polysulfide dissolution and shuttling are the main challenges that plague the long cycle life and capacity retention of lithium-sulfur (Li-S) batteries. To address these challenges, efficient separators are designed and modified with a dual functional bimetallic metal-organic framework (MOF). Flower-shaped bimetallic MOFs (i.e., Fe-ZIF-8) with nanostructured pores are synthesized at 35 °C in water by introducing dopant metal sites (Fe), which are then coated on a polypropylene (PP) separator to provide selective channels, thereby effectively inhibiting the migration of lithium polysulfides while allowing homogeneous transport of Li-ions. The active sites of the Fe-ZIF-8 enable electrocatalytic conversion, facilitating the conversion of lithium polysulfides. Moreover, the developed separator can prevent dendrite formation due to the uniform pore size and hence the even Li-ion transport and deposition. A coin cell using a Fe-ZIF-8/PP separator with S-loaded carbon cathode displayed a high cycle life of 1000 cycles with a high initial discharge capacity of 863 mAh g^{-1} at 0.5 C and a discharge capacity of 746 mAh g^{-1} at a high rate of 3 C. Promising specific capacity has been documented even under high sulfur loading of 5.0 mg cm^{-2} and electrolyte to the sulfur ratio (E/S) of 5 µL mg^{-1}.

1. Introduction

The ever-increasing dependence on portable/rechargeable energy sources and the urgent need for energy storage for renewable energy and the green transition has triggered a rapid development in battery technologies with long life, high-energy density, materials sustainability, and safety.[1] Currently, the rechargeable battery market is dominated by lithium-ion batteries (LiBs). However, after more than three decades of development, the LiBs are facing fundamental limitations in terms of energy density, safety, and cost. For example, electric vehicles still need to further upgrade the energy density to improve the driving range to at least 1000 km.[2] Hence, there is a tremendous effort to develop battery technologies that can meet this demand.

In this scenario, lithium-sulfur (Li-S) batteries are considered a ground-breaking technology because they have five times the theoretical specific capacity (1675 mAh g^{-1}) of LiBs with high specific energy density (2600 Wh kg^{-1}).[2b] However, a long-standing issue that hinders the practical implementation of Li-S batteries is the dissolution of intermediate polysulfides in organic electrolytes. These polysulfides migrate unimpededly through a highly porous separator (e.g., Celgard) toward the Li-anode, where they are further reduced on the Li-metal anode to form insoluble Li_2S/Li_2S_2, resulting in loss of active material and passivation of Li-metal anode.[3] Furthermore, the formation of the Li-dendrites due to uneven dissolution/deposition of Li may lead to internal short circuits and, consequently, explosion, which is a typical risk in lithium-based batteries.[3–4]

One of the well-accepted strategies to tackle the challenges to improve the performance of Li-S batteries has been to immobilize sulfur and polysulfides within a sulfur cathode, which is typically achieved by physically confining them in conductive carbon hosts as a cathode material.[5] However, the nonpolar carbon could not hold the polar polysulfides for a long time, leading to poor electrochemical performance.[6] Therefore, different kind of sulfur hosts has been designed to chemically confine the sulfur and polysulfides, such as conductive doped

R. Razaq, V. Eyupoglu, N. Allahgoli, L. Deng
Department of Chemical Engineering
Norwegian University of Science and Technology
Trondheim 7034, Norway
E-mail: rameez.razaq@ntnu.no; liyuan.deng@ntnu.no
M. M. U. Din, D. Rettenwander
Department of Materials Science and Engineering
Norwegian University of Science and Technology
Trondheim 7034, Norway
M. M. U. Din, D. Rettenwander
Christian Doppler Laboratory for Solid State Batteries
Norwegian University of Science and Technology
Trondheim 7034, Norway
D. R. Småbråten, S. Janakiram, T. O. Sunde
SINTEF Industry
Oslo 0373, Norway

The ORCID identification number(s) for the author(s) of this article can be found under https://doi.org/10.1002/aenm.202302897

DOI: 10.1002/aenm.202302897

carbon-based materials,[7] transition metal sulfides,[8] oxides,[9] single-atom catalysts,[10] and MXenes.[11]

Various strategies have also been taken to reduce or prevent the formation of Li-dendrites, such as by employing Li-metal alloys and artificial solid electrolyte interface (SEI) layers,[12] but not simultaneously. The synthesis of these materials usually involves a complex, high-temperature synthesis process involving expensive and toxic reagents. Therefore, it is desired to develop sustainable materials in a more cost-effective route for Li-S batteries that can simultaneously suppress the shuttling of polysulfides and lithium dendrite formation.

An intuitive solution to prevent polysulfide dissolution/shuttling and uneven deposition of Li-ions in Li-S batteries is to introduce a selective membrane, or separator, between the electrodes. In this regard, metal-organic frameworks (MOFs) can be a promising candidate due to their unique "size effects" on multiple molecular and ionic guests.[13] The unique sieving capability of MOF-based materials[14] inspired us to redesign it as an active separator for Li-S batteries with the multifunction of blocking and catalytic conversion of soluble polysulfides to prevent shuttling in rechargeable Li-S batteries.[15] The uniform sized MOFs also allow even and free transport of Li-ions. Previous studies have used various MOFs in modified separators,[16] but it is not sufficient to block polysulfides by the specific pore size of MOF material alone. In this regard, introducing a 2nd active metal site as an electrocatalyst for electro-catalytically converting the blocked or adsorbed polysulfides into active materials may be an effective solution.

Herein, we report a dual functional bimetallic three dimensional (3D) MOF-based separator designed specifically for Li-S batteries, which is expected to selectively block and convert polysulfides while providing even transport of Li-ions. ZIF-8 was selected as the parental MOF to construct the Fe-doped ZIF-8 (Fe-ZIF-8) to prepare the bimetallic MOF as the separator material because its 3D channel structure contains highly ordered micropores with pore sizes of ≈3.4 and ≈10Å,[17] which is significantly smaller than the diameters of intermediate chain length of lithium polysulfide;[18] thus, it is well suited for blocking polysulfides. At the same time, the dopant Fe sites are anticipated as an efficient electrocatalyst for the adsorption and conversion of polysulfides. Owing to the unique structural design, the Li-S batteries with Fe-ZIF-8 coated polypropylene (PP) as separators deliver the specific capacity even at a high current rate. Furthermore, it exhibits the extraordinary capacity retention of 92% after 100 cycles at 0.1 C with a high areal sulfur loading of 3.6 mg cm^{-2} and a low electrolyte/sulfur (E/S) ratio of 10 µL mg^{-1}. It is worth mentioning that the synthesis process of Fe-doped ZIF-8 is environmentally benign and cost-effective, using H_2O as the only solvent and synthesizing at merely 35 °C.

2. Results and Discussion

The flower shape 3D Fe-ZIF-8 was prepared by a one-step solution phase synthesis method using binuclear Fe and Zn paddle and methylimidazole linkers in H_2O at 35 °C (**Figure 1a**; Figure S1, Supporting Information). The structural integrity of ZIF-8 and Fe-ZIF-8 was demonstrated by the powder X-ray diffraction (PXRD) (Figure 1b). The PXRD clearly shows that the peak intensity of the Fe-ZIFs decreased slightly as compared to those of the parent ZIF-8, suggesting the loss of crystallinity during the metal exchange from Zn^{2+} to Fe^{2+}, which might be due to the octahedral coordination of Fe (II) into tetrahedral coordination.[19] Furthermore, a noticeable transformation in color from white (ZIF-8) to light brown (Fe-ZIF-8) was observed (insets of Figure 1b).

The morphology of the Fe-ZIF-8 was observed by scanning electron microscope (SEM). SEM images disclose that Fe-ZIF-8 exhibited incomplete formation of a flower-like structure when it was synthesized for 12 h (Figure S2, Supporting Information). However, it was found that more and more micro-sized flowers appeared when the reaction time increased, accompanying the significant decrease of irregular nanoplates, especially when the time was increased to 24 h (Figure 1c,d). The energy dispersive X-Ray (EDX) mapping of the Fe-ZIF-8 shows the presence of different elements (such as Zn, N, C, and Fe) (Figure 1e–h). Detailed structural characteristics of Fe-ZIF-8 have been extensively studied and are available in the literature.[17b,c,20] The parental ZIF-8 also shows a similar 3D flower-like structure with many ZIF-8 nanoplates, as can be seen in Figure S3 (Supporting Information).

Since the primary objective of developing the modified separator in the current work is to eliminate the polysulfide shuttling to improve the electrochemical performances in Li-S batteries, the modified separator should be able to block the shuttling of polysulfides and electro-catalytically convert the captured polysulfides, and also provide enough space for free transport of salt, solvents, and Li-ions across the separator. The structure and morphology of the separator were studied with respect to their effects on the transport properties of polysulfides and Li-ions. The digital images of the modified separator demonstrate that the PP separator is fully covered with Fe-ZIF-8 (Figure 1i). The Fe-ZIF-8 separator was twisted twice, but it has the ability to hold its initial shape, which implies that Fe-ZIF-8 is firmly bound to the separator and possesses high mechanical stability with sufficient flexibility (Figure 1j-l). The thickness of the coated layer on the separator was only ≈8 µm (Figure 1m). Furthermore, SEM images of the pristine PP separator (Figure S4, Supporting Information) and the Fe-ZIF-8/PP separator (Figure 1n) were performed. The PP separator contains a porous structure with pores in a wide range of up to several hundreds of nanometers, which allows the penetration of polysulfides dissolved in the electrolyte, while the SEM images of the Fe-ZIF-8 coated separator clearly show that the separator is fully coated with the Fe-ZIF-8 (Figure 1n). This coating is aimed to provide the pore structure and functionality that block polysulfides. The uniformly sized pores inside the MOFs should also prevent lithium dendrite formation. Thermal shrinkage of the separator is a significant factor in the safety characteristics of the battery. Unlike commercial separators, the Fe-ZIF-8 separator is exceptionally thermally stable and does not shrink when subjected to heating, e.g., up to 150 °C (Figure 1o–r). This superior thermal tolerance could prevent internal electrical short circuits at elevated temperatures during cell cycling.

Firstly, Li||Li symmetric cells were employed to evaluate the polarization effect by using PP, ZIF-8/PP, and Fe-ZIF-8/PP separators. The Li electrode with the PP separator exhibits a high initial overpotential (72 mV) at a current density of 0.5 mA cm^{-2} and an areal capacity of 1 mA h cm^{-2}. The Li electrode with the ZIF-8/PP separator shows a lower overpotential (38 mV).

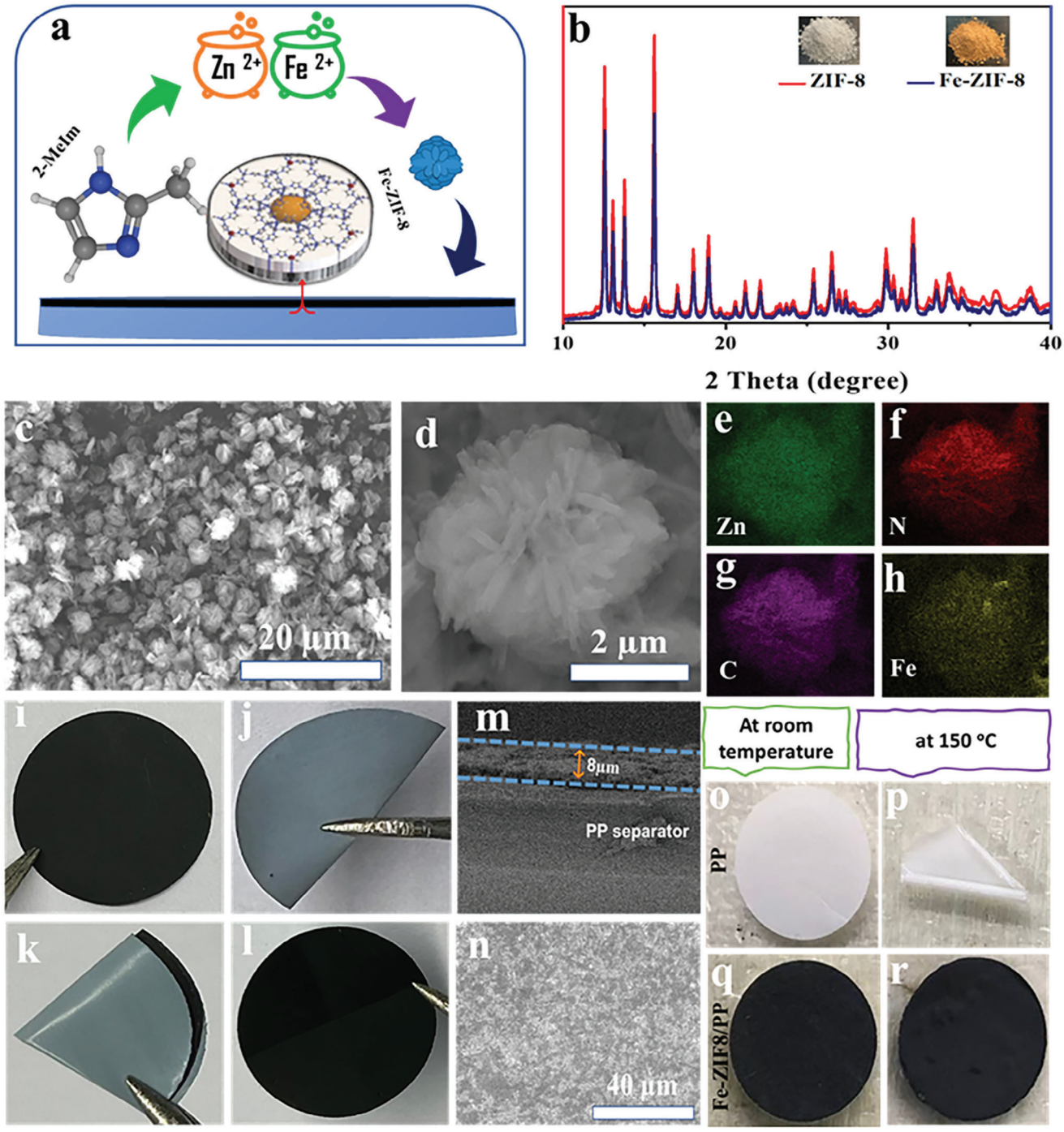

Figure 1. Schematic illustration for the preparation of Fe-ZIF-8 a). XRD pattern of ZIF-8 and Fe-ZIF-8 b), SEM images and EDX mapping of the Fe-ZIF-8 c–h). Digital images of Fe-ZIF-8 coated separator i), single and double folded j,k), and recovered l). Thickness measurement of the coated layer of Fe-ZIF-8 on PP m), SEM image of Fe-ZIF-8 coated on PP n). Thermal stability test of Fe-ZIF-8/PP and PP at room temperature and 150 °C (o-r).

However, the Fe-ZIF-8/PP battery delivers the minimum polarization (36 mV) (**Figure** 2a). Likewise, symmetric cells with the Fe-ZIF-8/PP separator also show steady polarization vibrations with increased current densities from 1 to 10 mA cm^{-2} under an areal capacity of 1 mA h cm^{-2} (Figure 2b,c). The voltage hysteresis of the symmetrical cell with the PP separator started to increase ≈700 h (Figure S5, Supporting Information), which is probably due to the growth of Li dendrites and the consumption of electrolytes. Figure 2d shows the ultra-long-term cycling performance of a symmetric cell with a Fe-ZIF-8/PP separator, which performed stably for more than 4000 h with a low voltage hysteresis. All these results confirm that the Fe-ZIF-8/PP

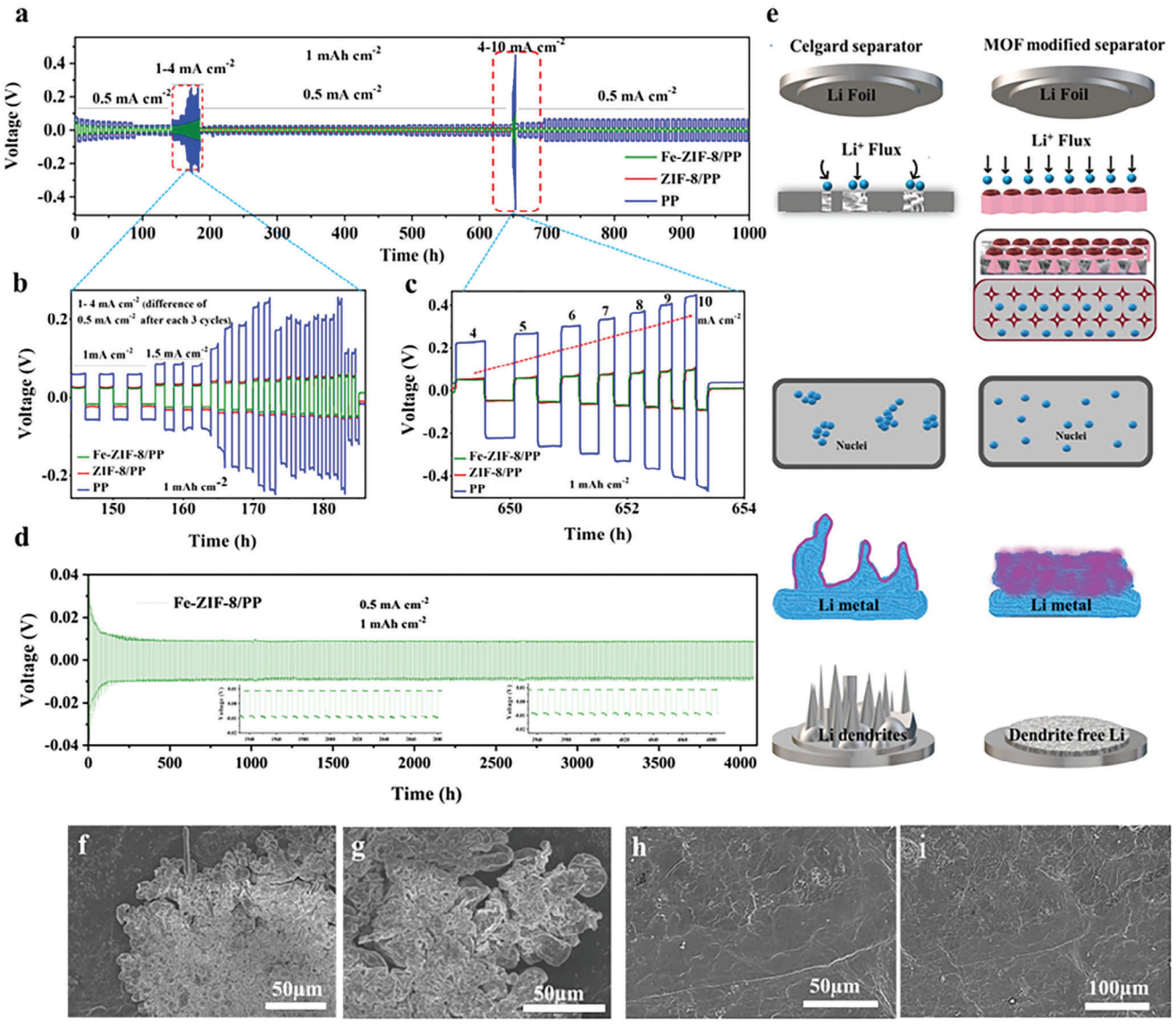

Figure 2. Li plating/stripping performance in symmetric cells with PP, ZIF-8/PP, and Fe-ZIF-8/PP separators at different current densities with an areal capacity of 1 mA h cm^{-2} a), the enlarged voltage profiles of PP, ZIF-8/PP, and Fe-ZIF-8/PP separators at the current densities of 1–4 mA cm^{-2} b), the enlarged voltage profiles of PP, ZIF-8/PP, and Fe-ZIF-8/PP separators at the current densities of 4–10 mA cm^{-2} c), and the Li plating/stripping behavior with an area capacity of 1 mA h cm cm^{-2} at 0.5 mA cm^{-2} ≈4000 h d). Schematics illustration of Li deposition on an electrode through a PP separator and through MOF channels (e). SEM images of Li anodes with PP separator f,g) and Fe-ZIF-8 protected PP separator h,i).

separator can promote uniform Li stripping and plating, which is highly desirable for the long-term cycle stability of the battery.

The effect of the Fe-ZIF-8/PP separator on promoting the uniform deposition of Li-ions is demonstrated by the surface evolution of the Li metal. The inhomogeneous Li-ion flux from the PP separator causes the overgrown Li dendrites due to the absence of uniform nanochannels, which also triggers the slow transport speed (Figure 2e). Benefitting from the ordered porous structure of Fe-ZIF-8, the homogeneous Li-ion flux from the Fe-ZIF-8/PP separator facilitates uniform Li plating on the Li electrode surface (Figure 2e). To reveal the role of Fe-ZIF-8/PP in the Li plating/stripping process, the surface morphologies of the plated Li after 1000 h cycles were examined by SEM. The surface of Li metal with a conventional PP separator presents cluttered Li dendrites (Figure 2f,g), but that with the Fe-ZIF-8/PP separator still maintains a smooth surface (Figure 2h,i), indicating a more effective function of the Fe-ZIF-8/PP separator in suppressing the growth of lithium dendrites.

High permeation resistance toward soluble polysulfides is critical for modified separators in Li-S batteries (**Figure 3a**). In this regard, the permeation experiment was conducted by using the H-type cell to examine the polysulfide permeation across the separators (Figure 3c,d). The polysulfide solution (0.1 M Li_2S_6) was added to the left side, and the blank electrolyte was introduced into the right side of the cell. The polysulfide permeation for the PP, ZIF-8/PP, and Fe-ZIF-8/PP modified

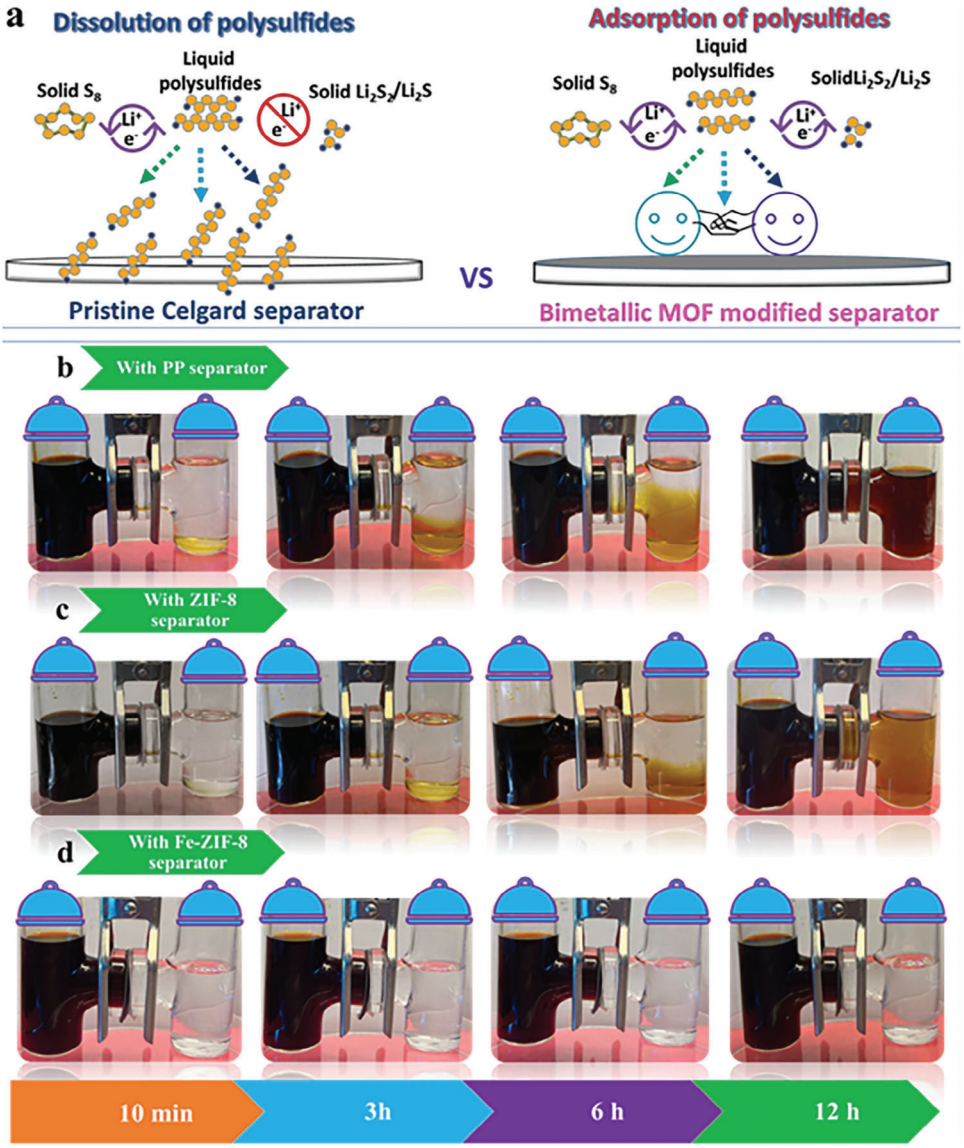

Figure 3. Schematics of the polysulfides permeation by PP and MOF modified separators a), polysulfide permeation test with PP separator, ZIF-8/PP separator, and Fe-ZIF-8/PP separator at different times c,d).

separator was investigated under similar conditions for different periods of time. For the PP separator, polysulfides diffuse to the right side of the H-cell quickly after 10 min, while for ZIF-8/PP, polysulfides diffused after 3 h, implying a poor capability of the highly porous PP separator in preventing the migration of polysulfides (Figure 3b,c). In contrast, the Fe-ZIF-8/PP separator demonstrates significant improvement in blocking the polysulfides. Even after 12 h, the polysulfide migration is still negligible, showing the superior polysulfide blocking capability of the Fe-ZIF-8/PP separator (Figure 3d). The permeation experiment was conducted for an extended time (24 h). As can be seen from Figure S6 (Supporting Information), only a nearly neglectable amount of polysulfide leakage was found toward the blank electrolytes. Nevertheless, during the charge/discharge, polysulfide conversion is expected to be more efficient during the cycling of cells, where only a controlled amount of polysulfides is formed in comparison to the permeation test with a flood of polysulfide. Therefore, such a small leakage is not a concern for the Li-S battery. The polysulfide permeability test confirms that the Fe-ZIF-8/PP separator has the ability to mitigate the shuttling of polysulfides (Figure 3d).

To provide further insight into the performance of the Fe-ZIF-8 modified separator, we have calculated the adsorption energies for relevant polysulfides in the sulfur reduction reaction (SRR) on the (001) surface using density functional theory (DFT) calculations (**Figure** 4a,b). Since Fe-segregation to the surface is not yet understood, we have investigated the effect of Fe present on the surface by varying the surface Fe content.

The (001) surface is formed by cleaving the metal(*M*)-N bonds,[21] resulting in an undercoordinated metal cation on the surface. The polysulfides are anchored to the surface by bonding between S anion and the undercoordinated metal cation

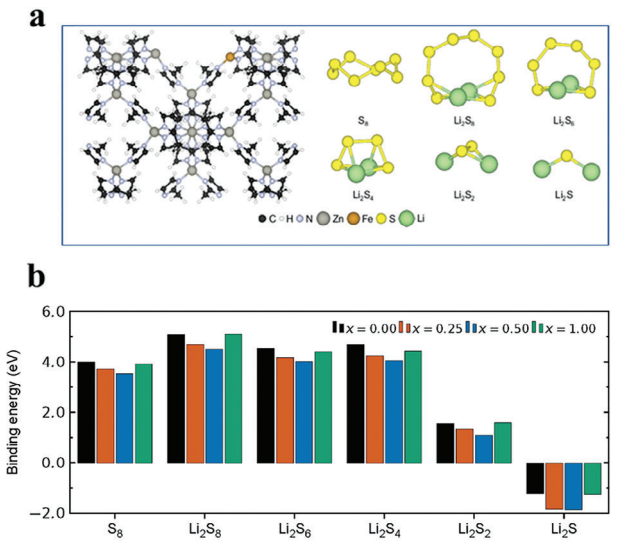

Figure 4. Illustration of the atomistic configurations of the ZIF-(Zn_{1-x},Fe_x)−8 (0 0 1) surface and S_8 and Li_2Sn (n = 8, 6, 4, 2, 1) along the SRR reaction path a), and calculated binding energies for the different adsorbates as a function of surface Fe-content x in ZIF-(Zn_{1-x},Fe_x)−8, b). Here, a positive binding energy implies a favorable binding interaction.

(Figures S7–S16, Supporting Information). All adsorbates except Li_2S are further stabilized by binding two S to two opposite metal cation sites. The resulting *M*-S bond lengths are in the range of 2.3–2.4 Å, which is comparable to the bulk Zn-N bond length of 2.0 Å. The polysulfides could, in principle, be anchored to the surface through Li-N bonding, as reported for 2D-MOFs.[22] This is, however, prohibited on the ZIF-8 (001) surface due to steric hindering. Note that chains of polysulfides have been reported to be anchored to the surface through *M*-S and O-Li bonds for an *M*-MOF (*M* = Ni, Co) with a comparable surface configuration to our system.[23] Here, we focus on the most commonly reported ring-like polysulfides only.

The binding energies for the different adsorbed polysulfides with varying surfaces' Fe contents are plotted in Figure 4b. The binding energies for S_8 and Li_2S_n (n = 8, 6, 4) range from 3.52 to 5.10 eV, suggesting a strong anchoring effect. The binding energy for Li_2S_2 ranges from 1.09 to 1.59 eV, suggesting a weaker anchoring effect, while the binding energies for Li_2S are negative and suggesting no anchoring effect. It is worth noting that the binding energies for Li_2S_2 and Li_2S are comparable to those for S_8 and Li_2S_n (n = 8, 6, 4) when using isolated molecules in vacuum as reference states (see Figures S16,S17, Supporting Information). To highlight the effect of Fe-substitution on the energetics, we first focus on the two endmembers, i.e., the fully Zn- and Fe-covered surfaces (x = 0.00 and x = 1.00, respectively). We find no significant difference in the adsorption energies for the two end members. Thus, Fe-substitution alone cannot explain any observed changes in permeation. This is also in agreement with observations for M_2(dobdc) (M = Fe, Zn) MOFs in literature.[24] The substitution of Zn with Fe gives only subtle changes in the surface structure, reasoned from the comparable ionic radii of Zn^{2+} and Fe^{2+} of 0.60 and 0.63, respectively. The comparable adsorption energetics could therefore be explained by similar surface structures. Interestingly, the intermediate compositions x = 0.25 and x = 0.50 show comparable energies that lie 0.2–0.5 eV lower in energy relative to the end members. Since the optimized configurations are comparable for all compositions, this suggests that there might be some systematic effect by having both cations on the surface of the adsorption energetics. We note that aliovalent substitution in, e.g., Al/Cu-MOFs has been reported to give significant surface reconstruction.[25] Fe can, in principle, possess multiple different oxidation states. However, we can safely assume that iron is in the Fe^{2+} oxidation state as for the bulk Fe-analogue of ZIF-8 (denoted MUV-3).

Common for all compositions investigated is that the polysulfides strongly bind the surface, with relatively subtle changes in adsorption energetics with respect to Fe-content. Hence, the changes in permeation with Fe-substitution (Figure 3a–d; Figure S8, Supporting Information) cannot be explained solely by changes in adsorption properties. Additional effects should also be investigated, i.e., bulk diffusion, rotation of the imidazolate rings,[26] and catalytic behavior; these will require further and extensive calculations in a separate theoretical study. A recent study on bulk Zn-ZIF-8, Mg-ZIF-8, and Fe-ZIF-8[26] suggested that Fe-ZIF-8 could allow for catalysis of reactions that require the direct involvement of the metal, such as the reactions on the electrode surfaces studied here.

The catalytic effects of the ZIF-8 and Fe-ZIF-8 electrodes were conducted on the redox conversion of polysulfides by cyclic voltammetry (CV) of symmetric cells within a Li_2S_6-containing electrolyte. Two pairs of distinct and highly reversible redox peaks (I, II, III, and IV) appeared for the battery with Fe-ZIF-8 counter and reference electrodes at −0.3 V, −0.02 V, 0.3 V, and 0.02 V, respectively (**Figure 5a**). Since upon polarization, it is assumed that in the anodic scan, Li_2S_6 was reduced to lower order polysulfides (Li_2S_2/Li_2S) at the working electrode (peak I), while oxidized to S on the counter electrode. In the anodic scan on the working electrode, Peak II shows the formation of Li_2S_6 by oxidation of Li_2S_2/Li_2S. Likewise, on the working electrode, peaks III and IV are identical in appearance to peaks I and II, showing the oxidation of Li_2S_6 to S and the reduction of S to Li_2S_6, respectively. Henceforth, the peaks at −0.3 V/0.02 V and −0.02 V/0.3 V were paired redox features of the symmetric cell. The overall reactions are summed up in Figure S17 (Supporting Information).[27]

In contrast, in the symmetric cells with ZIF-8 electrodes, redox peaks with broad features were detected. The dramatic increase in the current densities of Fe-ZIF-8-containing symmetric cells indicates that dopant Fe sites accelerate the catalytic conversion of polysulfides.

To further evaluate the catalytic transformation of sulfur species in a full cell, the electrochemical performance of Li-S batteries was investigated using PP, ZIF-8/PP, and Fe-ZIF-8/PP separators with Li as the anode and S-CNT/GO as the cathode (Figure S18, Supporting Information). The CV curves of Li-S batteries with PP, ZIF-8/PP, and Fe-ZIF-8/PP separators were examined under the voltage window of 1.7–2.8 V at a scan rate of 0.1 mV s^{-1}. Figure 5b shows two distinct reductions; peaks I and II are assigned to the conversion of S_8 molecule to high-order soluble polysulfides and their further transformation to Li_2S_2 and Li_2S. The oxidation peaks (III and IV) corresponded to the conversion of Li_2S_2 and Li_2S to the sulfur molecule. However, the CV curve of Fe-ZIF-8/PP showed two sharp redox peaks, i.e., the significant negative move of the oxidation peak and the positive move

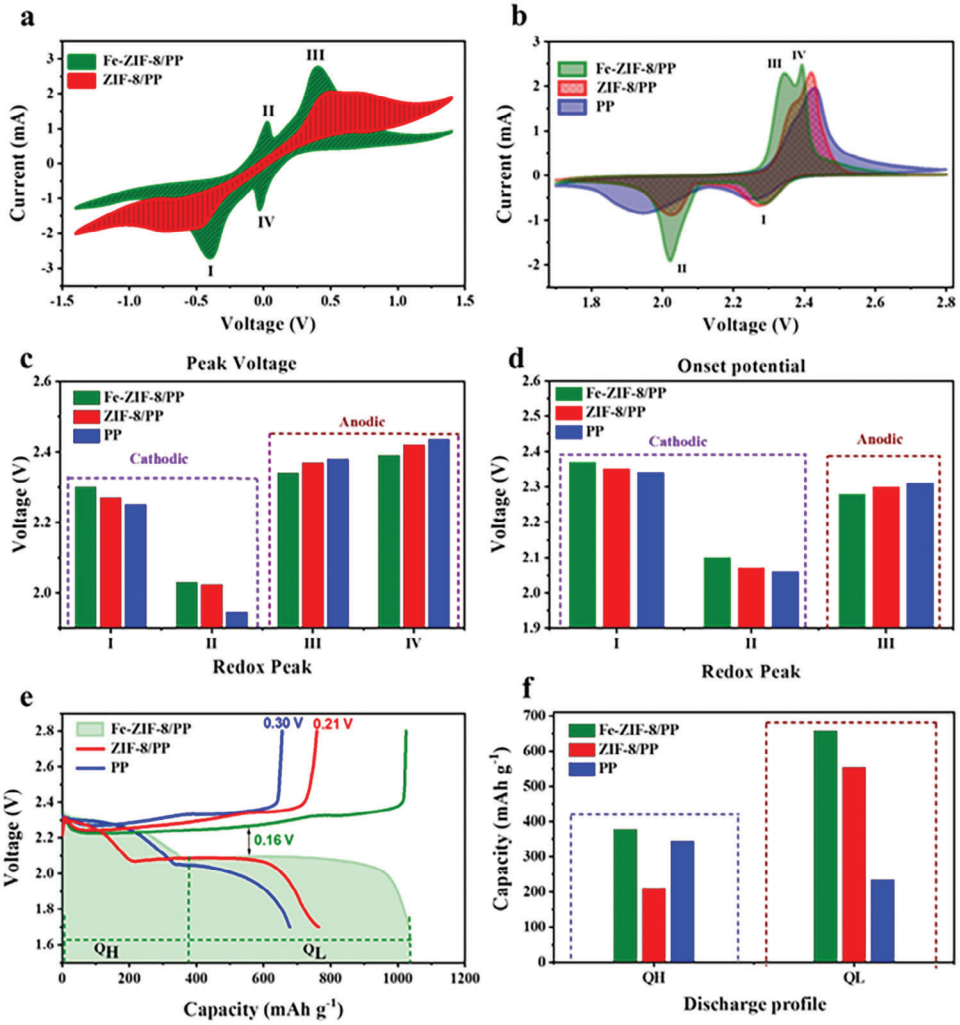

Figure 5. Electrocatalytic conversion of sulfur species. CV curves of the symmetric cells with the ZIF-8/PP and Fe-ZIF-8/PP electrodes in electrolytes with from −1.4 to 1.4 V a), CV profiles b), peak voltages c), and onset potential d), of the Li-S batteries based on PP, ZIF-8/PP, and Fe-ZIF-8/PP. Galvanostatic charge/discharge profiles e) and Q_H and Q_L capacities for the Li-S batteries based on PP, ZIF-8/PP, and Fe-ZIF-8/PP.

of the reduction peak, suggesting the reducing polarization and much better electrocatalysis, while the well-echoed peaks indicate the reversible electrochemical reactions that occurred in the electrode materials.[28] Furthermore, the variations in peak voltages and onset potentials for the reduction and oxidation peaks were obtained from CV. Figure 5c,d clearly shows the increase in cathodic peak intensities and a decrease in the anodic peaks for Fe-ZIF-8/PP in comparison with ZIF-8/PP and PP, suggesting the efficient conversion of the polysulfides, namely, electrocatalytic effects.

Electrochemical polarization was studied for Fe-ZIF-8/PP, ZIF-8/PP, and PP separators to further confirm the improved conversion of polysulfides. As shown in Figure 5e, the discharge plateaus of Li-S with Fe-ZIF-8/PP are flatter, along with a higher discharge and charge capacity. Moreover, Fe-ZIF-8/PP shows less voltage hysteresis ($\Delta E = 0.16$ V) compared with ZIF-8/PP ($\Delta E = 0.21$ V) and PP ($\Delta E = 0.30$ V). In the galvanostatic discharge curves, Q_H corresponds to the high discharge plateaus, and Q_L corresponds to the low discharge plateaus for the conversion reaction of the polysulfides. The Q_H and Q_L for Fe-ZIF-8/PP, ZIF-8/PP, and PP cell configurations are presented in Figure 5e,f. The Li-S battery with Fe-ZIF-8/PP displays the highest specific capacity for Q_H and Q_L compared with ZIF-8/PP and PP cells (Fe-ZIF-8/PP: Q_H: 378, Q_L: 658; ZIF-8/PP: Q_H: 210, Q_L: 545; PP: Q_H: 344, Q_L: 334 mAh g^{-1}). The high discharge capacity values for Q_H and Q_L confirm that the electrocatalytic conversion of the polysulfides improved the utilization of active material. Furthermore, the oxidation of Li_2S back to sulfur during battery charging is highly important in accomplishing high reversible capacity.[29] Compared with ZIF-8/PP (2.34 V), Fe-ZIF-8/PP considerably reduces the height of the potential barrier to 2.29 V (Figure S19, Supporting Information). The lower potential barrier in the case of Fe-ZIF-8/PP separator suggests that the charge transfer resistance and overpotential are reduced to a great extent.

These experimental results show a clear improvement in the electrocatalytic behaviors for the Fe-doped ZIF-8. To further study the effect of the Fe-content in the ZIF-8 on the sulfur SRR activity, we have calculated the reaction energies for

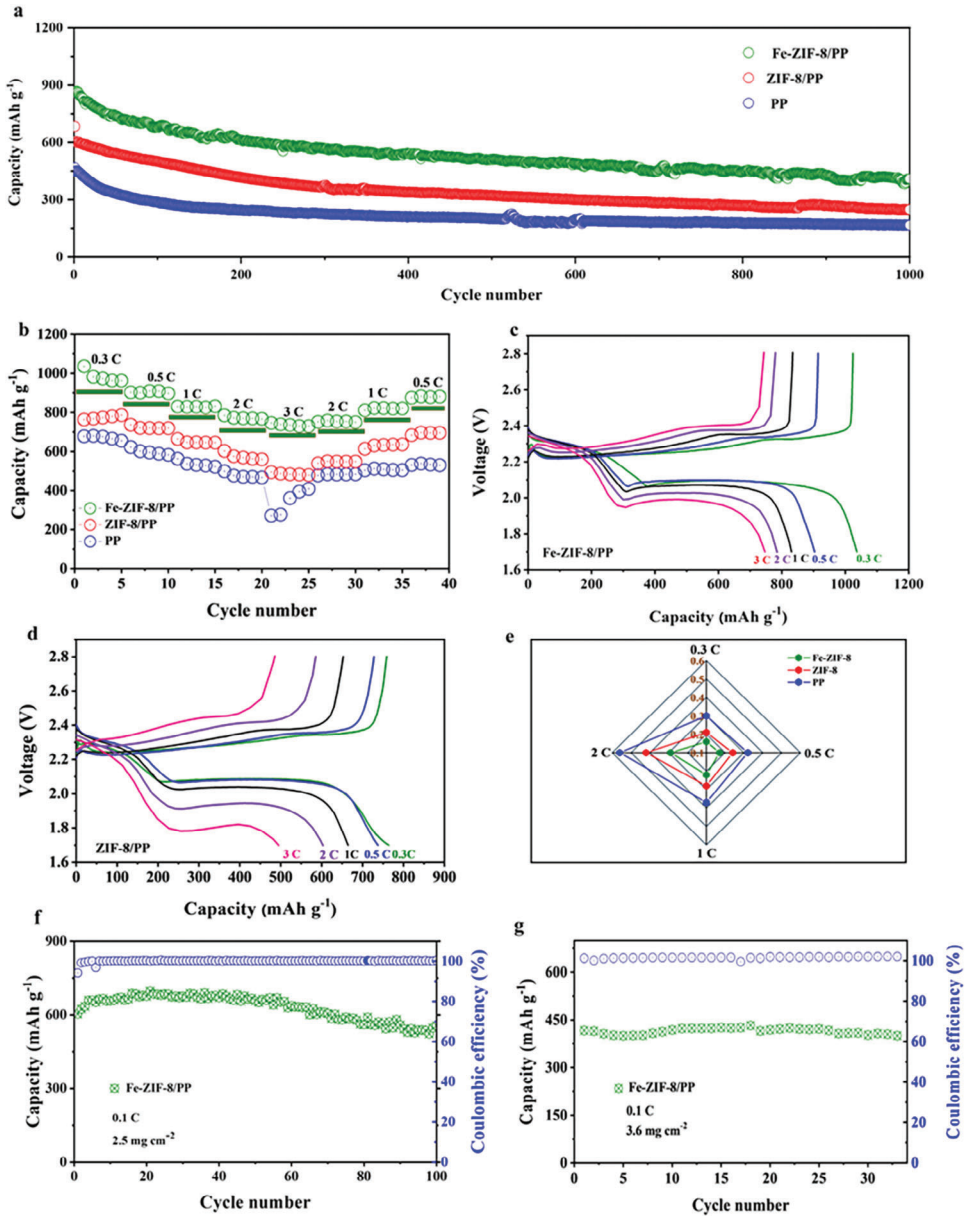

Figure 6. Energy-storage properties of the Li-S batteries with different separators. Long-term cycling performance of the Li-S batteries at 0.5 C a), The rate capability at different current densities b), Discharge and charge profiles at different Crates for Li-S batteries with ZIF-8/PP and Fe-ZIF-8/PP separators c,d), comparison of the voltage hysteresis for PP and ZIF-8/PP, Fe-ZIF-8/PP separators, and f) Cycling performance of Li-S batteries with Fe-ZIF-8/PP separators with a sulfur loading of 2.5 mg cm^{-2} and b) 3.6 mg cm^{-2}.

each elementary reaction step in the SRR as a function of the surface Fe-content. The energy diagrams are shown in Figure S20 (Supporting Information). Note that the energy diagrams are evaluated from the ground state energies of the reactants and products in each elementary reaction. This simplified approach will only provide a minimum value for the energy barrier for each elementary reaction step. To properly determine the electrocatalytic behavior, it would be necessary to calculate the minimum energy paths for intermediate atomic configurations along the elementary reaction steps. This requires further in-depth theoretical studies beyond the scope of the present work.

The Li-S batteries with PP and ZIF-8/PP, Fe-ZIF-8/PP separators, S-CNT/GO cathode, and Li anode were assembled into 2032-type coin cells, and their long-term cycling performances were evaluated. As shown in **Figure 6a**, Fe-ZIF-8/PP exhibits 865 mAh g^{-1} discharge capacity, ending with 409 mAh g^{-1} after 1000 cycles with a Coulombic efficiency of ≈100% at 0.5 C. The capacity fading in the initial 200 cycles can be associated with the release of sulfur from the cathode architecture due to volume expansion during cell discharge, which is a well-known phenomenon in Li-S batteries, leading to lower sulfur utilization due to accumulation of dead or non-conducting sulfur because of contact loss with conductive carbon. In contrast, Li-S batteries of ZIF-8/PP and PP

showed lower initial capacities (683 and 466 mAh g^{-1}), endings with 249 and 167 mAh g^{-1} after 1000 cycles, and Coulombic efficiency of 100%. (Figure S21, Supporting Information). Furthermore, rate capability was measured at different current rates (C-rates) to confirm the reversibility of the specific capacity. The battery with the PP separator showed dramatic capacity decay at different C-rates (Figure 6b). At 0.3 C, the initial capacity can reach up to 763 mA h g^{-1} for the ZIF-8 separator. On cycling at varied C-rates, namely 0.5 C, 1 C, 2 C, and 3 C, the capacities remained at 737, 664, 603, and 494 mA h g^{-1}, respectively. When the current density was switched back to 0.5, the capacity reverted to 640 mA h g^{-1}, showing 0.36% capacity decay per cycle. In contrast, the Li-S battery with Fe-ZIF-8 separator demonstrated much better performance (1036 mA h g^{-1} at 0.3 C). On cycling at 0.5 C, 1 C, 2 C, and 3 C, the capacities remained at 903 mAh g^{-1}, 830 mA h g^{-1}, 785 mA h g^{-1}, and 746 mA h g^{-1}, respectively. Finally, the capacity returned to 882 mA h g^{-1} at 0.5 C, while the capacity decay was merely 0.06% per cycle. In addition, discharge and charge voltage curves at various C-rates for selected cycles are shown in Figure 6c,d and Figure S22 (Supporting Information). All the discharge curves of Li-S batteries with Fe-ZIF-8 separators demonstrate two plateaus. Most importantly, the discharge curves show that even at 3C, the values of Q_H and Q_L were high and clearly visible with the lowest voltage hysteresis for Fe-ZIF-8, but the discharge and charge plateaus with the ZIF-8, and particularly with the PP separator, are not obvious at 3 C. Moreover, the voltage hysteresis for ZIF-8 and PP are quite high with the increase of the current rate compared with Fe-ZIF-8 (Figure 6e). Most importantly, cell performance was measured at 50 °C, confirming the best cycling performance at elevated temperatures (Figure S23, Supporting Information).

For the commercialization of Li-S batteries, addressing the challenge of achieving high sulfur loading is crucial. Up to now, most of the researchers could gain high capacity and long cycle life when under low areal sulfur loadings <1.0 mg cm^{-2} while using a high amount of electrolyte. In the current work, to deal with this problem, the areal sulfur loading was increased from 2.5 to 5.0 mg cm^{-2} by fabricating a thick electrode. The Li-S batteries with 2.5 mg cm^{-2} areal sulfur loading and electrolyte to the sulfur ratio of 10 µL per mg of sulfur exhibited a 603 mAh g^{-1} discharge capacity, ending with 555 mAh g^{-1} after 100 cycles at the Coulombic efficiency of ≈100% with 92% capacity retention (Figure 6f; Figure S24, Supporting Information). Similarly, with an areal loading of 3.6 mg cm^{-2}, Li-S batteries with Fe-ZIF-8/PP showed a 92% capacity retention after 33 cycles (Figure 6g; Figure S25, Supporting Information). Furthermore, areal loading of sulfur was increased to 5.0 mg cm^{-2}, and the electrolyte to sulfur ratio was reduced to 5 µL mg^{-1}. Surprisingly, without engineering the cathode structure, Li-S battery with Fe-ZIF-8/PP separator could deliver capacity around 517 mAh g^{-1} at 0.05 C (Figure S26, Supporting Information). Henceforth, the developed dual functional bimetallic 3D MOF-based separator containing active functional sites is an effective approach to selectively block and convert the dissolved polysulfides and efficiently reduce the lithium dendrite formation, resulting in improved overall battery performance.

To prove the stability of coated separators, the cycled cell is disassembled (disassembling was performed inside the glove box), and the separator was removed and washed with DME solvent. After subsequent drying at 50 °C in the glove box, the digital image and SEM-EDS of the separator of the separator has shown an intact MOF coating, which confirms the mechanical stability of the separator during cycling (See Figure S27, Supporting Information). While EDS analysis of modified separator toward the anode side clearly shows the neglectable amount of polysulfides migration (Figure S28, Supporting Information).

For the readers' convenience, the performance data of the Li-S batteries with Fe-ZIF-8 coated separator in this work and similar battery systems published in leading journals are summarized in Table S1 (Supporting Information). Li-S batteries with a coating thickness of only 8 µm of Fe-ZIF-8 on PP separator shows the capacity decay of merely 0.05% per cycle after 1000 cycles at 0.5 C. Furthermore, the sustainability of the material in terms of synthesis strategy, temperature, and capacity retention at high areal loading are compared in Table S2 (Supporting Information).

3. Conclusion

A novel, cost-effective 3-D bimetallic Fe-ZIF-8 modified separator with designed functionalities was developed to selectively block and convert the dissolved polysulfides while sieving Li-ions in Li-S batteries. Remarkably higher catalytic activity was observed for the conversion of polysulfides by the Fe-doped ZIF-8 compared to the parent ZIF-8. Meanwhile, incorporating Fe (II) centers into the ZIF framework dramatically improved the specific capacity and rate capability. The Li-S battery using Fe-ZIF-8/PP separator displays a high cycle life of 1000 cycles and exhibits a high initial capacity of 863 mAh g^{-1} at 0.5 C and 746 mAh g^{-1} at 3 C. Furthermore, the Fe-ZIF-8/PP separator delivers desirable sulfur electrochemistry even under the relevant conditions of high sulfur loading and lean electrolyte. At the same time, Li||Li symmetrical cell with Fe-ZIF-8/PP separator exhibited outstanding cycling performance at a high current density of up to 10 mA cm^{-2}. These encouraging results validated the unique sieving capability of the Fe-ZIF-8/PP separator with the synergistic effects of blocking and catalytic conversion of soluble polysulfides to prevent shuttling in rechargeable Li-S batteries while allowing free and uniform transport of Li-ions. Furthermore, it also sheds light on the development of 3-D bimetallic MOF-based materials as modified separators for other metal-sulfur battery applications.

4. Experimental Section

Synthesis of Bimetallic ZIF-8 and Fe-Doped ZIF-8: ZIF-8 was synthesized following the following steps:

1) Dissolving the $ZnSO_4 \bullet 7H_2O$ (575 mg) in 30 mL of water and 1.314 g of 2-Methylimidazole in 30 mL of water in another beaker.
2) Stir the solutions for several minutes at room temperature and add the metal solution into the solution of 2-Methylimidazole followed by continuously stirring for 24 h at 35 °C.
3) The white precipitate in the beaker was collected by centrifugation, washed with DI water, and dried for 12 h at 70 °C. The Fe-doped ZIF-8 was synthesized by the same method, however, $FeSO_4 \bullet 7H2O$ (46.3 mg) was also added to the aqueous solution of $ZnSO_4 \bullet 7H_2O$ in step 1. The subsequent steps are the same as with ZIF-8. The obtained samples were labeled as ZIF-8 and Fe- ZIF-8.

Fabrication of Modified Separator: ZIF-8 and Fe- ZIF-8 modified separators were engineered by coating the slurry containing ZIF-8 and Fe-ZIF-8, Super P, and PVDF onto the Celgard 2400. Briefly, the slurry was prepared by mixing Fe- ZIF-8, Super-P, and PVDF in NMP in a weight ratio of 75:15:10, respectively, and ball milled in a sealed Teflon jar for ≈40 min. The obtained slurry was cast onto a Celgard 2400 separator and dried at 60 °C for 12 h. After drying, the modified separator was punched into a round shape with a diameter of 19 mm.

Preparation of Sulfur Electrodes: Sulfur was loaded in CNT/GO (1:1) by the conventional melt-diffusion method. In brief, sulfur powder and CNT/GO were thoroughly mixed by grinding and then sealed in a glass vial. The glass vial was then transferred inside the autoclave and heated at 155 °C for 12 h. The slurry for the cathode was fabricated by mixing S-CNT/GO powder (90 wt.%) with a PVDF binder (10 wt.%) using NMP as the solvent. The obtained slurry was then cast onto carbon-coated Al foil by the doctor's blade and dried at 60 °C for 12 h to prepare electrodes. Finally, the electrodes were cut into 12 mm discs. The areal sulfur loading in the resultant cathode is in the range of 1–5.0 mg cm^{-2}.

Electrochemical Measurement: Common CR2032-type coin cells were assembled inside an argon-filled glovebox consisting of a sulfur cathode, MOF-modified Celgard separator, and a Li foil anode. The electrolyte contained 1 M LiTFSI and 0.1 M $LiNO_3$ in 1:1 (v/v) 1,2-dimethoxyethane (DME) and 1,3-dioxacyclopentane (DOL). For comparison, the coin cell with the pristine separator was also prepared. The charge/discharge voltage range was 1.7–2.8 V. The rate performance was also tested by varying the current density from 0.1 to 3 C (1 C = 1675 mA g^{-1}). The CV tests were performed on an electrochemistry workstation (SP-300) at a scan rate of 0.1 mVs^{-1}.

Assembly of Li_2S_6 Symmetric Cells: Li_2S_6 symmetric cells were assembled by using identical electrodes working simultaneously as the anode and the cathode. The slurry for the electrode was made by mixing ZIF-8 and Fe-ZIF 8, super P with PVDF in NMP with a mass ratio of 8:1.1 using a ball mill for 40 min, and then the slurry was coated on the Al foil and dried at 60 °C for 24 h. Finally, prepared electrodes were punched into 12 mm discs. Two identical electrodes as the cathode and anode were assembled into a 2032-coin cell with Li_2S_6 electrolyte and Celgard separator. The electrolyte containing Li_2S_6 was prepared by dissolving Li_2S and S with a molar ratio of 5:1 in DM/EDOL under continuous stirring for 12 h. The electrolyte also contained 0.15 mol L^{-1} $LiNO_3$ and 0.50 mol L^{-1} LiTFSI. CV was performed on an electrochemical workstation. CV was performed at a scan rate of 1 mV s^{-1} in a voltage window from −0.14 to 0.14 V.

Materials Characterization: XRD patterns were recorded on Bruker AXS D8 ADVANCE (from 2005) X-ray Diffractometer with Cu$K\alpha$ radiation and a Våntec-1 SuperSpeed detector using 40 kV as tube voltage and 40 mA as tube current. The morphology of the samples was investigated by S(T)EM, (Hitachi High-Tech SU9000) mode equipped with field emission scanning electron microscopy. TGA (Netzsch TG209F1) was performed to determine the weight ratio of the components in the samples.

Density Functional Theory Calculations: DFT calculations were performed using the projector augmented wave (PAW) as implemented in VASP.[30] The calculations were carried out with a plane-wave cutoff energy of 550 eV and an electronic convergence criterion of 10^{-5} eV. C (2s, 2p), H (1s), N (2s, 2p), Zn (4s, 3d), Fe (4s, 3p, 3d), S (3s, 3p), and Li (1s, 2s) were treated as valence electrons. The PBE+U[31] functional with U = 4 eV applied to Fe 3d was used, benchmarked to the density of states calculations on bulk ZIF-8 and Fe(II) analogue to ZIF-8 (denoted MUV-3) using HSE06 (see Figures S13,S14, Supporting Information).[32] The neighboring Fe-sites were anti-ferromagnetically coupled. Long-range interactions were described by the DFT-D3 method.[33] The (0 0 1) surface was modelled by a 276 atoms thick slab, where the 4 bottom atomic layers were fixed during structural optimization. The periodic images were separated by a 25 Å vacuum region, including dipole corrections to reduce spurious interactions. Adsorption was modeled on the $c(1\times1)$ surface. The references for S_8 and Li_2S_n (n = 8, 6, 4) were modelled as isolated molecules in vacuum in a 20×20×20 Å simulation box, while the references for Li_2S_2 and Li_2S were modelled by their solid phases.[34] Atomic positions were relaxed until the residual forces on all atoms were below 0.05 eV $Å^{-1}$. The binding energies were calculated by $E_B = E_{MOF}+E_{LiP}-E_{ads}$, where E_{MOF} are the energies for the clean MOF surfaces, E_{LiP} the reference energies for the lithium polysulfides, and E_{ads} the energies for the adsorbed systems.[22b] The overall SRR $S_8 + 16Li^+ + 16e^- \rightarrow 8Li_2S$ was modelled by the following elementary reaction steps.[22b]

$$*S_8 + 2Li^+ + 2e^- \rightarrow * Li_2S_8 \quad (1)$$

$$* Li_2S_8 \rightarrow * Li_2S_6 + \frac{1}{4}S_8 \quad (2)$$

$$* Li_2S_6 \rightarrow * Li_2S_4 + \frac{1}{4}S_8 \quad (3)$$

$$* Li_2S_4 \rightarrow * Li_2S_2 + \frac{1}{4}S_8 \quad (4)$$

$$* Li_2S_2 \rightarrow * Li_2S + \frac{1}{8}S_8 \quad (5)$$

where * refers to an adsorbed species on the surface.

Supporting Information

Supporting Information is available from the Wiley Online Library or from the author.

Acknowledgements

This work is supported by the Research Council of Norway (No. 327193) and (No. 349916) and the M-ERA.NET 2020 call.

Conflict of Interest

The authors declare no conflict of interest.

Data Availability Statement

The data that support the findings of this study are available from the corresponding author upon reasonable request.

Keywords

adsorption, bimetallic MOF, dendrite formation, electrocatalyst, lithium-sulfur batteries, polysulfide shuttle

Received: August 30, 2023
Revised: November 4, 2023
Published online: November 21, 2023

[1] D. Larcher, J.-M. Tarascon, *Nat. Chem.* **2015**, *7*, 19.
[2] a) J. T. Frith, M. J. Lacey, U. Ulissi, *Nat.Commun* **2023**, *14*, 420; b) G. Zhou, H. Chen, Y. Cui, *Nat. Energy* **2022**, *7*, 312.
[3] L.-P. Hou, X.-Q. Zhang, B.-Q. Li, Q. Zhang, *Mater. Today* **2021**, *45*, 62.
[4] Z. Wang, Y. Li, H. Ji, J. Zhou, T. Qian, C. Yan, *Adv. Mater.* **2022**, *34*, 2203699.
[5] M. Zheng, Y. Chi, Q. Hu, H. Tang, X. Jiang, L. Zhang, S. Zhang, H. Pang, Q. Xu, *J. Mater. Chem. A* **2019**, *7*, 17204.
[6] H. Wang, W. Zhang, J. Xu, Z. Guo, *Adv.Funct. Mater.* **2018**, *28*, 1707520.

[7] a) A. K. Thakur, K. Kurtyka, M. Majumder, X. Yang, H. Q. Ta, A. Bachmatiuk, L. Liu, B. Trzebicka, M. H. Rummeli, *Adv. Mater. Interfaces* **2022**, *9*, 2101964; b) M. Sun, X. Wang, Y. Li, Z. Zhao, J. Qiu, *Appl. Catal. B* **2022**, *317*, 121763.
[8] a) R. Razaq, N. Zhang, Y. Xin, Q. Li, J. Wang, Z. Zhang, *Chem. Select* **2020**, *5*, 7563; b) R. Razaq, D. Sun, J. Wang, Y. Xin, G. Abbas, J. Zhang, Q. Li, T. Huang, Z. Zhang, Y. Huang, *J. Power Sources* **2019**, *414*, 453; c) W. Hua, T. Shang, H. Li, Y. Sun, Y. Guo, J. Xia, C. Geng, Z. Hu, L. Peng, Z. Han, C. Zhang, W. Lv, Y. Wan, *Nat. Catal.* **2023**, *6*, 174.
[9] a) Z. He, T. Wan, Y. Luo, G. Liu, L. Wu, F. Li, Z. Zhang, G. Li, Y. Zhang, *Chem. Eng. J.* **2022**, *448*, 137656; b) R. Razaq, D. Sun, Y. Xin, Q. Li, T. Huang, Z. Zhang, Y. Huang, *Adv. Mater. Interfaces* **2019**, *6*, 1801636; c) X. Liang, C. Y. Kwok, F. Lodi-Marzano, Q. Pang, M. Cuisinier, H. Huang, C. J. Hart, D. Houtarde, K. Kaup, H. Sommer, T. Brezesinski, J. Janek, L. F. Nazar, *Adv. Energy Mater.* **2016**, *6*, 1501636.
[10] a) L. Ren, J. Liu, Y. Zhao, Y. Wang, X. Lu, M. Zhou, G. Zhang, W. Liu, H. Xu, X. Sun, *Adv. Funct. Mater.* **2023**, *33*, 2210509; b) T. Huang, Y. Sun, J. Wu, Z. Shi, Y. Ding, M. Wang, C. Su, Y.-Y. Li, J. Sun, *Adv. Funct. Mater.* **2022**, *32*, 2203902; c) X. Meng, X. Liu, X. Fan, X. Chen, S. Chen, Y. Meng, M. Wang, J. Zhou, S. Hong, L. Zheng, G. Shi, C. W. Bielawski, J. Geng, *Adv. Sci.* **2022**, *9*, e2103773.
[11] a) X. Zhong, D. Wang, J. Sheng, Z. Han, C. Sun, J. Tan, R. Gao, W. Lv, X. Xu, G. Wei, X. Zou, G. Zhou, *Nano Lett.* **2022**, *22*, 1207; b) X. Li, Q. Guan, Z. Zhuang, Y. Zhang, Y. Lin, J. Wang, C. Shen, H. Lin, Y. Wang, L. Zhan, L. Ling, *ACS Nano* **2023**, *17*, 1653; c) Y. He, Y. Zhao, Y. Zhang, Z. He, G. Liu, J. Li, C. Liang, Q. Li, *Energy Storage Mater.* **2022**, *47*, 434.
[12] H. Hong, N. A. R. Che Mohamad, K. Chae, F. Marques Mota, D. H. Kim, *J. Mater. Chem. A* **2021**, *9*, 10012.
[13] a) Y. Zheng, S. Zheng, H. Xue, H. Pang, *J. Mater. Chem. A* **2019**, *7*, 3469; b) N. Yuan, W. Sun, J. Yang, X. Gong, R. Liu, *Adv. Mater. Interfaces* **2021**, *8*, 2001941; c) J. Zeng, K. Charyulu Devarayapalli, S. V. Prabhakar Vattikuti, J. Shim, K. Charyulu Devarayapalli, S. V. Prabhakar Vattikuti, J. Shim, *Mater. Lett.* **2022**, *309*, 131305.
[14] J. Zeng, K. C. Devarayapalli, S. V. P. Vattikuti, J. Shim, *Int. J. Energy Res.* **2021**, *46*, 6031.
[15] a) Z. Zhu, Y. Zeng, Z. Pei, D. Luan, X. Wang, X. W. (D.) Lou, *Angew. Chem. Int. Ed. Engl.* **2023**, *62*, e202305828; b) X. Hu, T. Huang, G. Zhang, S. Lin, R. Chen, L.-H. Chung, J. He, *Coord. Chem. Rev.* **2023**, *475*, 214879; c) M.-T. Li, N. Kong, Y.-Q. Lan, Z.-M. Su, *Dalton Trans.* **2018**, *47*, 4827.
[16] a) H. Chen, Y. Xiao, C. Chen, J. Yang, C. Gao, Y. Chen, J. Wu, Y. Shen, W. Zhang, S. Li, F. Huo, B. Zheng, *ACS Appl. Mater. Interfaces* **2019**, *11*, 11459; b) C. Qi, L. Xu, J. Wang, H. Li, C. Zhao, L. Wang, T. Liu, *ACS Sustainable Chem. Eng.* **2020**, *8*, 12968; c) X. Leng, J. Zeng, M. Yang, C. Li, S. V. P. Vattikuti, J. Chen, S. Li, J. Shim, T. Guo, T. J. Ko, *J. Energy Chem.* **2023**, *82*, 484.
[17] a) S. Bai, B. Kim, C. Kim, O. Tamwattana, H. Park, J. Kim, D. Lee, K. Kang, *Nat. Nanotechnol.* **2021**, *16*, 77; b) X. Gong, K. Gnanasekaran, Z. Chen, L. Robison, M. C. Wasson, K. C. Bentz, S. M. Cohen, O. K. Farha, N. C. Gianneschi, *J. Am. Chem. Soc.* **2020**, *142*, 17224; c) Y. Li, K. Wang, W. Zhou, Y. Li, R. Vila, W. Huang, H. Wang, G. Chen, G.-H. Wu, Y. Tsao, H. Wang, R. Sinclair, W. Chiu, Y. Cui, *Matter* **2019**, *1*, 428.
[18] M. Rana, M. Li, X. Huang, B. Luo, I. Gentle, R. Knibbe, *J. Mater. Chem. A* **2019**, *7*, 6596.
[19] L. E. Mphuthi, E. Erasmus, E. H. G. Langner, *ACS Omega* **2021**, *6*, 31632.
[20] J. López-Cabrelles, J. Romero, G. Abellán, M. Giménez-Marqués, M. Palomino, S. Valencia, F. Rey, G. Mínguez Espallargas, *J. Am. Chem. Soc.* **2019**, *141*, 7173.
[21] S. H. Pang, C. Han, D. S. Sholl, C. W. Jones, R. P. Lively, *Chem. Mater.* **2016**, *28*, 6960.
[22] a) Y. Li, S. Lin, D. Wang, T. Gao, J. Song, P. Zhou, Z. Xu, Z. Yang, N. Xiao, S. Guo, *Adv. Mater.* **2020**, *32*, 1906722; b) J. Wang, F. Li, Z. Liu, Z. Dai, S. Gao, M. Zhao, *ACS Appl. Mater. Interfaces* **2021**, *13*, 61205.
[23] J. Zheng, J. Tian, D. Wu, M. Gu, W. Xu, C. Wang, F. Gao, M. H. Engelhard, J.-G. Zhang, J. Liu, J. Xiao, *Nano Lett.* **2014**, *14*, 2345.
[24] H. Park, D. J. Siegel, *Chem. Mater.* **2017**, *29*, 4932.
[25] P. Geng, M. Du, X. Guo, H. Pang, Z. Tian, P. Braunstein, Q. Xu, *Energy Environ. Mater.* **2021**, *5*, 599.
[26] J. G. Vitillo, L. Gagliardi, *Chem. Mater.* **2021**, *33*, 4465.
[27] H. Lin, L. Yang, X. Jiang, G. Li, T. Zhang, Q. Yao, G. W. Zheng, J. Y. Lee, *Energy Environ. Sci.* **2017**, *10*, 1476.
[28] a) C. Zhang, R. Du, J. J. Biendicho, M. Yi, K. Xiao, D. Yang, T. Zhang, X. Wang, J. Arbiol, J. Llorca, Y. Zhou, J. R. Morante, A. Cabot, *Adv. Energy Mater.* **2021**, *11*, 2100432; b) Z. Liang, D. Yang, P. Tang, C. Zhang, J. Jacas Biendicho, Y. Zhang, J. Llorca, X. Wang, J. Li, M. Heggen, J. David, R. E. Dunin-Borkowski, Y. Zhou, J. R. Morante, A. Cabot, J. Arbiol, *Adv. Energy Mater.* **2020**, *11*, 2003507.
[29] G. Zhou, H. Tian, Y. Jin, X. Tao, B. Liu, R. Zhang, Z. W. Seh, D. Zhuo, Y. Liu, J. Sun, J. Zhao, C. Zu, D. S. Wu, Q. Zhang, Y. Cui, *Proc. Natl. Acad. Sci. U S A* **2017**, *114*, 840.
[30] a) P. E. Blöchl, *Phys. Rev. B Condens Matter* **1994**, *50*, 17953; b) G. Kresse, J. Furthmüller, *Phys. Rev. B Condens Matter* **1996**, *54*, 11169.
[31] a) J. P. Perdew, K. Burke, M. Ernzerhof, *Phys. Rev. Lett.* **1996**, *77*, 3865; b) S. L. Dudarev, G. A. Botton, S. Y. Savrasov, C. J. Humphreys, A. P. Sutton, *Phys. Rev. B* **1998**, *57*, 1505.
[32] A. V. Krukau, O. A. Vydrov, A. F. Izmaylov, G. E. Scuseria, *J. Chem. Phys.* **2006**, *125*, 224106.
[33] S. Grimme, J. Antony, S. Ehrlich, H. Krieg, *J. Chem. Phys.* **2010**, *132*, 154104.
[34] H. Park, H. S. Koh, D. J. Siegel, *J. Phys. Chem. C* **2015**, *119*, 4675.